An automatic procedure for calibrating the fracture parameters of fibre-reinforced concrete

F. Suárez[a], J. Donaire[a], J. F. Aceituno[a]

[a]*Department of Mechanical and Mining Engineering. Universidad de Jaén. Campus Científico-Tecnológico de Linares. Cinturón Sur 23700-Linares (Jaén)*

Abstract

In this work a calibration procedure to obtain the material parameters that characterize the fracture behaviour of fibre-reinforced concrete (FRC) is presented. This procedure uses a recently proposed trilinear softening diagram implemented in a smeared crack model of the free finite element code OOFEM that allows reproducing the fracture behaviour of FRC and takes advantage of the optimization package of SciPy, with both pieces of software being open-source and of free access for anyone interested in this field. This work presents the calibration procedure, which uses the Nelder-Mead algorithm to adjust the numerical result with the experimental diagram and discusses some key aspects, such as the number of reference points used in the calibration process or the weighting factors used with them, including the possibility of making some reference points more relevant than others in the calibration process. The influence of the mesh size and the element type used in the FEM model is also analysed. To evaluate the quality of the numerical approximation, a deviation factor is defined, which provides an scalar value that becomes lower as the numerical adjustment is closer to the experimental diagram in the reference points. The proposed procedure allows calibrating six parameters automatically with a meaningful time reduction and good accuracy. Using a higher number of reference points may lead to a better adjustment, although this study suggests that a good selection of the reference points is more effective than using a high number of reference points or using weighting factors to make some points more relevant than others. This procedure is finally validated by applying it with experimental results obtained with other types of FRC materials (different fibres and different fibre proportions) and specimen geometries.

Keywords: Fibre-reinforced concrete, Parameter calibration, OOFEM, SciPy, Fracture.

Nomenclature

*F. Suárez
Email address: fsuarez@ujaen.es (F. Suárez)

Lower case

w	crack opening value
w_i	crack opening at point i of the trilinear diagram
h	crack band thickness
f_i	stress at point i of the trilinear diagram
$\boldsymbol{x_i}$	i^{th} vertex of the simplex in the Nelder-Mead method

Upper case

$\boldsymbol{D}$	stiffness tensor
$\boldsymbol{D}_e$	elastic stiffness tensor
E	material elastic modulus
G_f	fracture energy
P_{num}	numerically obtained load value
P_{exp}	experimentally obtained load value

Greek

α	reflection coefficient in the Nelder-Mead method
γ	expansion coefficient in the Nelder-Mead method
δ	load displacement
ε_0	strain at the onset of fracture
ε_{eq}	equivalent strain
λ	deviation factor
λ_0	value of the deviation factor at the first iteration
ρ	contraction coefficient in the Nelder-Mead method
$\bar{\sigma_I}$	Ith principal stress
ω	damage

1. Introduction

The use of fibre-reinforced concrete (FRC) is not new [1], but has experienced a big impulse in recent years, mainly by the addition of practical guidelines in the main structural standards used by designers and contractors of structures [2, 3, 4, 5] . The increasing interest in FRC has produced a remarkable number of experimental studies to identify how diverse aspects of their production affect their properties, both in fresh state and hardened. Together with these experimental studies, several approaches have been proposed for numerically reproducing fracture in FRC [6, 7, 8, 9, 10]. It is worth mentioning the use of cohesive fracture by using a trilinear softening diagram [11] that allows reproducing the behaviour of this material taking into account different FRC mixes (with different fibre length and proportion), different loading scenarios [12] and capturing the size effect [13]. Moreover, the trilinear softening diagram is defined with crack opening and stress values that are related with physical parameters of the FRC mix (concrete strength, fibre length and polymer elastic modulus or the fibre proportion, for instance). The trilinear softening diagram is defined by six values (f_t, f_k, f_r, w_k, w_r and w_f), that correspond to stresses (f_i) and crack opening values (w_i) that must be calibrated to fit the experimental results. The values of the parameters in the softening diagram can be obtained through inverse analysis, where experimental test results from notched laboratory specimens are used to calibrate the parameters of the diagram in a numerical model involving non-linear analyses. This process fits the numerical and experimental—reference—force-displacement or force-crack mouth opening displacement curves. Accordingly, two calibration approaches are proposed in the literature: the first of them is based on fitting the area under the reference curves [14, 15, 16] and the second one on selecting specific points from the reference curves [17, 18, 19, 20, 21, 22]. Since this process includes a relatively high number of parameters to adjust, it implies carrying out a trial and error process that may lead to a high number of models to be run (typically, around 25 would be a fair estimation). This type of softening diagram has been successfully used with an embedded fracture model in the past [11, 13, 23] and has been recently

implemented in a smeared crack fracture model of the free finite element code OOFEM [24, 10]. In this work, the six parameters that define the trilinear softening diagram, which characterizes the material's fracture behaviour, are calibrated by using specific points from the reference experimental curve. This process is automated by using the Nelder-Mead optimization algorithm, which is part of the optimization package in SciPy [25].

This work is divided as follows: the second section presents the objective by briefly describing the smeared crack model used in the numerical simulations and the trilinear softening diagram that uses the six parameters that must be calibrated. In the third section, the calibration procedure is described, including the definition of the deviation factor that is used to compare the numerical result with the experimental curve that must be approximated, and a brief description of the Nelder-Mead minimisation algorithm employed to calibrate the material parameters. In the fourth section, in order to illustrate the performance of this algorithm, an experimental reference of a three-point bending test is used and, by providing the experimental load-displacement diagram and an initial set of parameter values, the algorithm calibrates the model; three main aspects of the calibration procedure are analysed in subsection 4.1: i) the influence of the number of reference points used for calibration, ii) the possibility of using different weighting factors with the reference points and iii) the influence of the selected reference points on the numerical adjustment. Subsection 4.2 analyses the influence of the mesh, mainly focusing on the element size and the element type used, on the calibration result, while subsection 4.3 validates the calibration procedure by applying it using experimental results obtained with different specimen geometries, different fibres and different fibre proportions. Therefore, unlike other studies like those cited before, this work conducts an in-depth analysis of the impact of the number and selection of control points used for comparing numerical and experimental curves, offering a more refined approach to automatic calibration. Finally, the fifth section enumerates the main conclusions of this work.

2. Objective

The objective of this work is to develop a calibration procedure to obtain a set of parameters that defines the fracture behaviour of FRC and analyse some aspects involved in it, such as the control points used for reference and the relevance of the mesh in the calibration result.

While the fracture behaviour of plain concrete can be described by only two parameters, namely the fracture energy (G_f) and the tensile strength (f_t), FRC needs more parameters to be defined and, depending on the type of fibres and their material, it may need as many as six. In the case of polyolefin fibre reinforced concrete, for instance, which exhibits one of the more complex fracture behaviours of FRC, these parameters are f_t, f_k, f_r, w_k, w_r and w_f, which identify the coordinates of four points that define a trilinear stress-crack opening diagram (σ - ω diagram). As Fig. 1 illustrates, point t identifies the tensile strength at which damage begins, point k corresponds to the end of the load drop after the initial load peak, when fibres start to show a meaningful contribution, point r is the point at which the fibre reinforcement begins to decay and point f identifies the point of complete damage, when fibre-reinforcement is no longer effective.

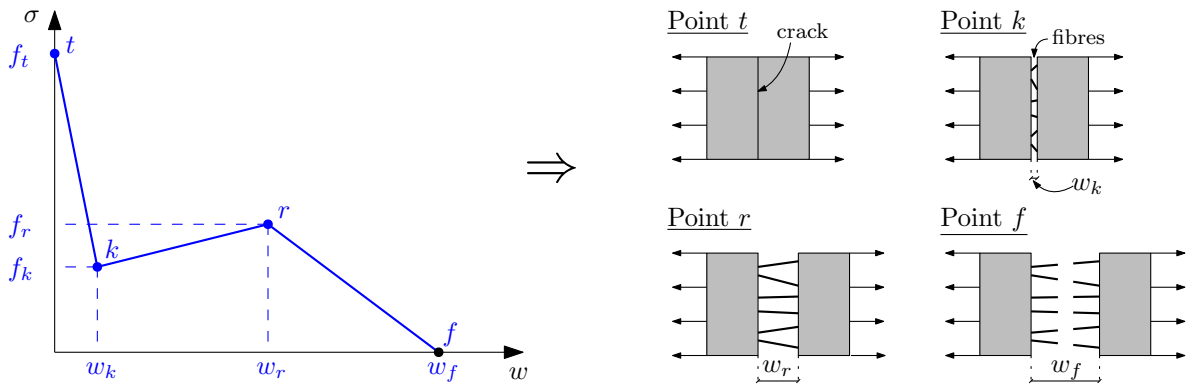

Figure 1: Trilinear softening diagram used to define the fracture behaviour of FRC.

2.1. Smeared crack model

In this work, the proposed calibration procedure has been applied to adjust the six parameters mentioned above that define the fracture behaviour of FRC through the trilinear diagram shown in Fig. 1. To do this, an isotropic damage formulation implemented in the open-source software OOFEM is used, a short description is provided here, although the complete description of the model can be found in [10].

In this model, damage is numerically induced in the material by means of the damage parameter ω, which ranges from 0 (no damage) to 1 (fully damaged) and degrades the material strength through the stiffness tensor as follows:

$$\boldsymbol{D} = (1 - \omega)\, \boldsymbol{D}_e \tag{1}$$

where D_e stands for the elastic stiffness tensor.

Damage is related to the material strain, to do this, an equivalent strain value is computed with the strain tensor, in this study the following expression of the equivalent strain, based on the Rankine criterion, is used:

$$\varepsilon_{eq} = \frac{1}{E}\sqrt{\sum_{I=1}^{3}\langle\bar{\sigma_I}\rangle^2} \tag{2}$$

The value of the damage parameter ω is computed for each part of the trilinear diagram by using the following expressions [1]:

- Between points t and k:

$$\omega = \frac{E}{E + h\left(\dfrac{f_k - E\varepsilon_0}{w_k}\right)} - \frac{E\varepsilon_0}{\varepsilon_{eq}\left[E + h\left(\dfrac{f_k - E\varepsilon_0}{w_k}\right)\right]}$$

- Between points k and r:

$$\omega = \frac{E}{E + h\left(\dfrac{f_r - f_k}{w_r - w_k}\right)} + \frac{1}{\varepsilon_{eq}} \cdot \frac{w_k\left(\dfrac{f_r - f_k}{w_r - w_k}\right) - f_k}{E + h\left(\dfrac{f_r - f_k}{w_r - w_k}\right)}$$

- Between points r and f:

$$\omega = \frac{E}{E + h\left(\dfrac{-f_r}{w_f - w_r}\right)} + \frac{1}{\varepsilon_{eq}} \cdot \frac{w_r\left(\dfrac{-f_r}{w_f - w_r}\right) - f_r}{E + h\left(\dfrac{-f_r}{w_f - w_r}\right)}$$

where E stands for the elastic modulus of concrete, ε_0 for the strain at which f_t is reached ($\varepsilon_0 = f_t/E$) and h is the crack width, which is obtained by projecting the finite element onto the direction of the maximum principal strain at the onset of damage, as suggested by Oliver [26], which ensures that the fracture process is adjusted to the element size and that the dissipated energy is correct.

Thus, considering E as a given value, and since h depends on the geometry of the finite element and is computed for each element through the numerical simulation process, six parameters must be calibrated to describe the fracture behaviour of FRC: ε_0, f_k, f_r, w_k, w_r and w_f.

[1] Note that symbol ω stands for damage and letter w represents crack opening.

3. Automatic calibration procedure

This section describes the calibration procedure. The first subsection describes the input data that is required by the procedure, the second subsection defines the deviation factor, which is used to estimate the validity of the calibration result in each iteration, and the third subsection presents the algorithm that performs the automated calibration procedure through a function that provides the value of the deviation factor, which is minimized using the Nelder-Mead optimization method.

3.1. Input data

The objective of the calibration procedure is to obtain a set of material parameters (ε_0, f_k, f_r, w_k, w_r and w_f) that allows reproducing the experimental behaviour of a FRC specimen with a numerical model. Therefore, three main items are necessary to feed the calibration procedure:

- An experimental result that needs to be adjusted, for example a load-displacement diagram.
- A base finite element model that reproduces the experimental test that needs to be reproduced. This model reproduces the geometry and the boundary conditions of the problem, but the material characteristics are not defined, since their definition is the purpose of the calibration process.
- Initial values of the parameters that are to be calibrated in order to start the process.

3.2. Deviation factor

Once the initial model is defined, it provides a numerical result that is compared with the experimental diagram. A scalar value called λ is defined to compare the numerical and the experimental diagrams and provide a quantity that can be compared in subsequent iterations so it can be minimized. This value will be referred hereinafter as deviation factor, which helps comparing the numerical and experimental load values at specific reference points and is defined as follows:

$$\lambda = \frac{\sum ||y_{i,exp} - y_{i,num}||}{\sum y_{i,exp}} \cdot weight_i \tag{3}$$

where $y_{i,exp}$ represents the experimental load at reference displacement i, $y_{i,num}$ the corresponding numerical load at reference displacement i (see Fig. 2) and $weight_i$ allows to obtain a weighted value where some reference points may have a higher influence than others on the calibration result.

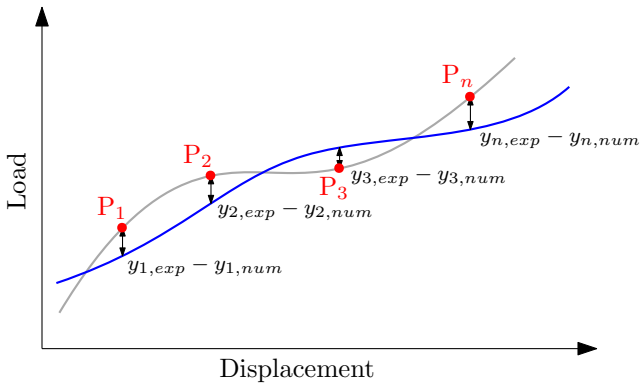

Figure 2: Deviation factor is obtained by evaluating the difference between the numerical and experimental diagrams at especific points throughout the test.

3.3. Calibration algorithm

To adjust the six parameters that define the material behaviour, the Nelder-Mead method is used [27]. This method is selected since it does not require any further information about the function to minimize, as some other methods do, such as the Dogleg algorithm, the Newton conjugate gradient trust-region algorithm or the Newton GLTR trust-region algorithm, among others, that need the Jacobian [28, 29], which is unavailable in this case.

The Nelder-Mead method makes use of a simplex and evaluates the function at each vertex; the method can be summarized in the following steps:

- Initialisation and ordering: the function is evaluated at each vertex of the simplex and ordered from best (minimum value) to worst (maximum value)

$$f(\boldsymbol{x_1}) \leq f(\boldsymbol{x_2}) \leq \cdots \leq f(\boldsymbol{x_n})$$

- Reflection: a reflection point is obtained by computing the centroid of all vertices ($\boldsymbol{x_0}$), excluding the worst (highest function value) and reflecting it through the worst vertex:

$$\boldsymbol{x_r} = \boldsymbol{x_0} + \alpha(\boldsymbol{x_0} - \boldsymbol{x_n}) \text{ with } \alpha > 0$$

  If the reflection point returns a better value than the second worst vertex but not better than the best, next simplex is obtained by replacing the worst vertex with the reflection point.

- Expansion: if the reflection point returns a better value than the best vertex, an expansion point is obtained beyond the reflection point:

$$\boldsymbol{x_e} = \boldsymbol{x_0} + \gamma(\boldsymbol{x_r} - \boldsymbol{x_0}) \text{ with } \gamma > 1$$

  If the expansion point returns a better value than the reflection point, it replaces the worst vertex in the new simplex.

- Contraction: if the reflection point returns a worse value than the second-worst vertex but better that the worst, a contraction point is obtained:

$$\boldsymbol{x_c} = \boldsymbol{x_0} + \rho(\boldsymbol{x_n} - \boldsymbol{x_0}) \text{ with } 0 < \rho \leq 1$$

- Shrink: if all previous operations do not lead to an improved simplex, a new simplex is defined by moving all vertices towards the best vertex.

All these possible operations are depicted in the schematic representation of Fig. 3, which corresponds to a simplex of a two-dimensional space, which allows easy representation.

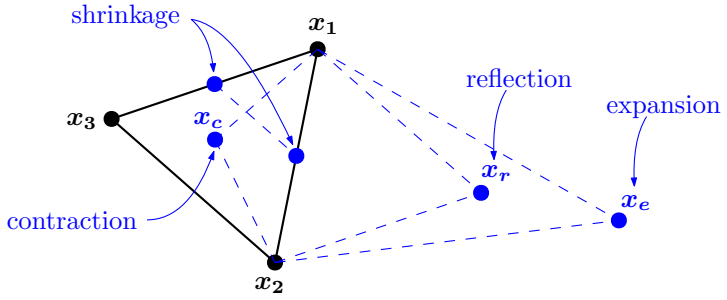

Figure 3: Scheme of the possible operations in the Nelder-Mead algorithm.

Therefore, the Nelder-Mead method needs a function to minimize and a set of parameters to adjust. Since the objective of this procedure is to minimize the deviation factor defined by Eq. 3, a function that computes the deviation factor for a specific set of parameters is defined. Table 1 describes the performance of this function, which receives a base FEM model, a set of parameters to evaluate and an experimental diagram

for comparison. The FEM model is modified with the set of the material parameters and is computed, producing a numerically obtained diagram, which is compared with the experimental one, thus returning an scalar value, which corresponds to the deviation factor defined before in Eq. (3).

Table 1: Basic scheme of the function to be minimized by the Nelder-Mead method.

`compute_dev_factor`
Input
• Base FEM model • Set of parameters: $(\varepsilon_0, f_k, f_r, f_t, w_k, w_r)_0$ • Experimental diagram
Output
• Deviation factor: $\lambda = \frac{\sum \lvert\lvert y_{i,exp} - y_{i,num} \rvert\rvert}{\sum y_{i,exp}} \cdot weight_i$

An scheme of the proposed calibration procedure is shown in Fig. 4a; elements in blue represent the data that is initially provided as given values. A base FEM model, which describes the geometry and the boundary conditions, is given together with an initial guess of the material parameters to adjust $(\varepsilon_0, f_k, f_r, w_k, w_r, w_f)_0$. The FEM model is initially modified so that the material behaviour is described by the initial guess of the parameters and is computed producing a load-displacement diagram. This numerically obtained diagram is compared with the experimental one and a deviation factor value is obtained as output. Then, the iteration process begins using the Nelder-Mead algorithm described before, which progressively modifies each of the six material parameters to minimize the value of the deviation factor, $(\varepsilon_0, f_k, f_r, w_k, w_r, w_f)_i$ represents the set of parameters used in the i^{th} iteration. In this work, no convergence criterion has been defined and the process is carried out up to 200 iterations in order to observe the consistency of the procedure.

3.4. Calibration result validation based on the released energy

In some studies, the criterion to validate the calibration result is based on comparing the released energy during the fracture process [15, 16, 14]. To do this, the error is defined as the difference between the area under the experimental and the numerically obtained curves, as expressed by Eq. (4).

$$error(\%) = \frac{\left|\int_0^{\delta_{max}} (P_{num} d\delta)\right| - \left|\int_0^{\delta_{max}} (P_{exp} d\delta)\right|}{\left|\int_0^{\delta_{max}} (P_{exp} d\delta)\right|} \cdot 100 \tag{4}$$

where P_{num} and P_{exp} stand for the numerical and experimental load values, respectively, and δ for the load displacement. Therefore, this expression computes the relative difference between the areas under the load-displacement diagram obtained experimentally and numerically, using the experimental area as reference. Figure 4b shows both areas for one of the cases analysed in this study, where the experimental area is presented in red and the numerical area in blue. This error is computed in this study in each of the analysed cases to validate the accuracy of the calibrated models. According to [16], an error under 2% is considered as a good fit.

4. Results and discussion

In this section the result of the described calibration procedure is analysed, including the comparison of several alternatives that will be detailed here. In all cases, the numerical model reproduces a notched specimen subjected to a three-point bending test; results of subsections 4.1 and 4.2 use the same specimen geometry, while subsection 4.3 uses different geometries extracted from other experimental campaigns.

Susbsection 4.1 analyses some aspects of the calibration process, especially the influence of the reference points and their weights on the computation of the deviation factor λ. Subsection 4.2 studies the influence

a)

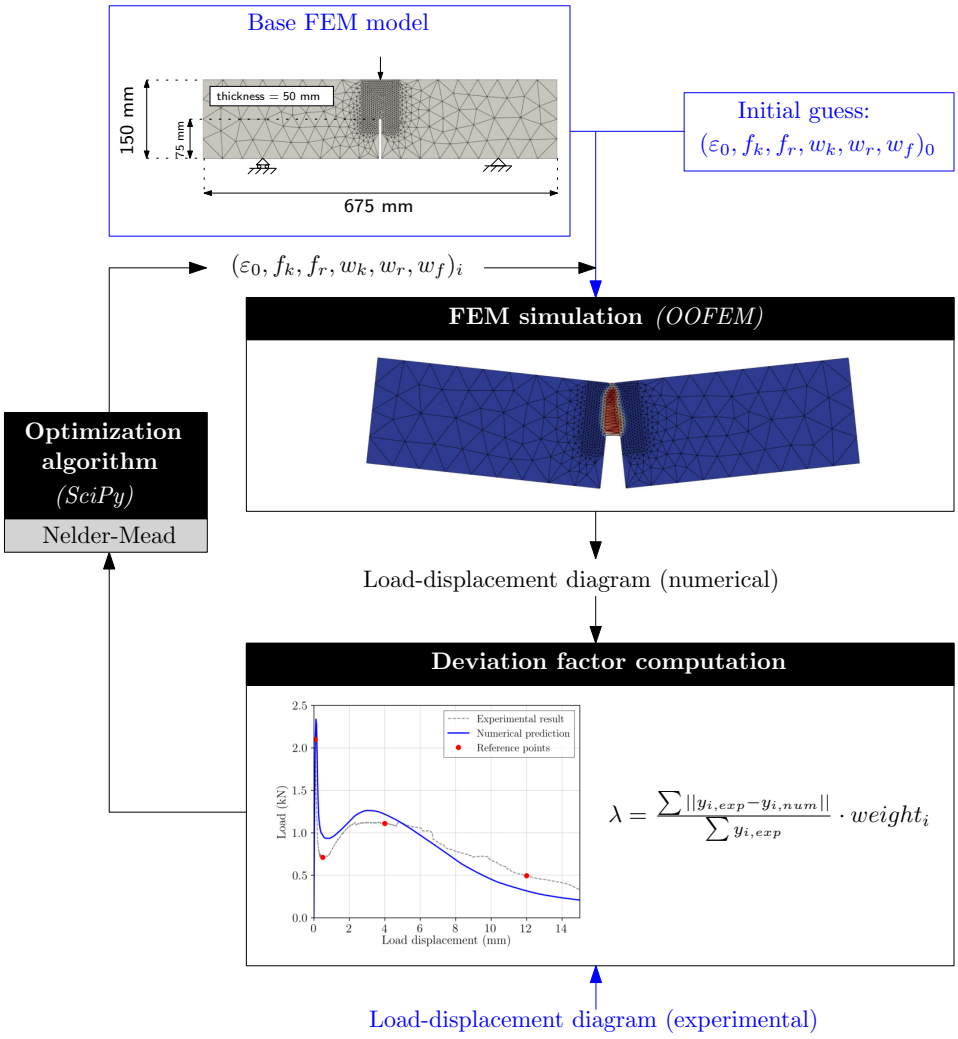

b)

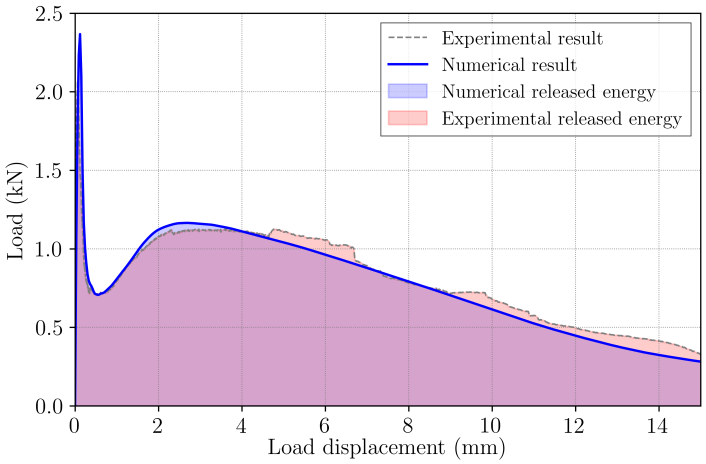

Figure 4: a) Scheme of the calibration algorithm. b) Computation of the difference between the experimental and numerical released energies

of key aspects of the mesh used in the model, more specifically, the element size in the region of fracture and the type of element used. Finally, Section 4.3 presents results of the calibration process on other specimen geometries and fibre-reinforced materials, using different proportions of polyolefin fibres and of steel fibres.

4.1. Influence of the control points selection and their weights

The choice of the selection points and their weights on the computation of the deviation factor, which determines the accuracy of the calibration, may result in different results. This section analyses how the selection of these points and the possibility of making some of them more relevant than others by means of using weights to compute λ may affect the calibration result.

To do this, the experimental diagram of one of the medium-size specimens in [30] is used. The base FEM model used in the calibration process is the same as the one used in [13], which reproduces the three point bending test on a specimen of 675 mm in length, 150 mm in height and 50 mm in thickness, with a notch of 75 mm at the center of the specimen, as shown in Fig. 4a. The mesh is refined in the region where crack develops with elements of 3.5 mm in size.

In all the cases that will be presented here, the initial values of the material parameters that are to be calibrated are: $\varepsilon_0 = 1.418 \cdot 10^{-4}$, $f_k = 0.57$ MPa, $f_r = 1.18$ MPa, $w_k = 0.09$ mm, $w_r = 1.65$ mm and $w_f = 6.0$ mm. In order to avoid incoherent values of the material parameters through the calibration process, such as defining negative values or incompatible values (for example, w_r must always be greater than w_k, as shown in Fig. 1), the following ranges were specified for each parameter, so they could not be assigned values out of these bounds: $\varepsilon_0 \in [1 \cdot 10^{-4}, 1 \cdot 10^{-2}]$, $f_k \in [0.1, 1.5]$, $f_r \in [0.1, 2]$, $w_k \in [0.01, 0.5]$, $w_r \in [1, 3]$ and $w_f \in [4.5, 8]$, with stresses expressed in MPa and crack openings in mm.

Another important aspect to consider in the calibration process is related to the points that are used as reference in the experimental diagram to compare the numerical result. As it has been described above, the quality of the numerical simulation is assessed in each iteration through the deviation factor defined by Eq. 3, which evaluates the difference between the numerical and the experimental diagrams at given points. The definition of the deviation factor also allows considering different weights depending on the relevance of the reference point, for example, some points may be more representative of the experimental diagram, such as those identifying the initial peak load, the initial load drop, the maximum subsequent load recovery and the final branch of load decay (they are marked with red dots in Fig. 4a). Therefore, the influence of three aspects on the calibration result are analysed here: firstly, the number of reference points used, secondly, the effectiveness of using different weights on the reference points to make some points more relevant in the final result and, finally, the relevance of using carefully selected reference points, since it is not clear *a priori* if using a high number of reference points will significantly improve the result of the calibration or a lower number of points may provide better results if they are wisely selected.

In this analysis, seven approaches will be used to compute the deviation factor, which serves as the calibration criterion:

- **Approach 1**: four reference points are used, which are related with four key aspects of the load-displacement diagram: peak load, initial load drop, maximum recovery load and final load drop branch. All reference points have the same weight (=1) on the computation of the deviation factor.
- **Approach 2**: 100 reference points are used, evenly distributed along the displacement axis. All reference points have the same weight (=1) on the computation of the deviation factor.
- **Approach 3**: all reference points of Approach 1 and Approach 2 are used. All reference points have the same weight (=1) on the computation of the deviation factor.
- **Approach 4**: the four key reference points of Approach 1 are used with a weight of 1.0 and the 100 evenly distributed reference points of Approach 2 with a weight of 0.5.
- **Approach 5**: the four key reference points of approach 1 are used with a weight of 1.0 and the 100 evenly distributed reference points of Approach 2 with a weight of 0.25.
- **Approach 6**: Using the four key reference points of Approach 1 with a weight of 1.0 and the 100 evenly distributed reference points of Approach 2 with a weight of 0.1.

- **Approach 7**: Using the four key reference points of Approach 1 and ten additional selected points at displacement values of 0.05, 0.15, 0.2, 0.25, 0.7, 1.5, 2, 2.5, 6 and 10 (expressed in mm).

The first three approaches help to understand how the selection of the reference points may be important in order to obtain a good calibration of the material parameters. Approaches 4 to 6 analyse if the use of different weights on the reference points, thus considering some of them more relevant than others in the calibration process, have an important effect on the result. Finally, Approach 7 helps to understand if using carefully selected reference points, rather than using a high number of points or varying the weighting factor on some of them, may help to produce a better adjustment.

In subsection 4.1.1 the first aspect is analysed using the results of approaches 1 to 3, in subsection 4.1.2 the influence of the weights selected for the more relevant points is analysed using the results of approach 3 to 6 and, finally, in subsection 4.1.3 the use of carefully selected reference points, rather than using many, is explored.

In all the diagrams shown hereinafter, the experimental results will be presented in grey, the results obtained with Approaches 1, 2 and 3 with solid lines in blue, green and magenta, respectively. As for the results obtained with Approaches 4, 5 and 6, dashed lines in blue, green and magenta, respectively, will be employed and results of Approach 7 will be presented in solid black lines. Finally, the reference points used in each approach will be depicted as red dots.

4.1.1. Influence of the number of selected reference points

Using Approaches 1 to 3, which, as described above, use different reference points to compare the numerical and experimental result in order to compute the deviation factor λ that is used by the Nelder-Mead minimisation algorithm, provide the trilinear diagrams observed in Fig. 5, that produce the load-displacement diagrams shown in Fig. 6. In general, all three approaches provide a good enough adjustment to the experimental diagram, depicted with a dashed grey line; the overall shape of the diagram can be considered as a good approximation of the experimental result, although some relevant differences can be observed. At a first glance, all three approaches provide a good approximation of the remanent peak after the initial load drop; in all cases, this second peak is almost the same, although it takes place at different displacement values; this is clearly related to the w_r parameter in the trilinear diagram if the trilinear diagrams and the load-displacement curves are analysed. All three approaches also provide a good approximation of the diagram after this second load peak.

If the initial part of the load-displacement diagram is analysed, interesting differences are observed. The initial peak is clearly different in each case. Approach 1, which only uses four reference points in the calibration process, clearly overestimates this peak load, while Approach 2 underestimates it and Approach 3 provides the most accurate approximation. Regarding the load decay after the initial peak, all three approaches provide a good enough approximation, although Approach 2 leads to a slightly higher value of the load. In any case, Approach 3 seems to provide the best approximation, since the other two approaches have a lack of accuracy around the peak load.

Fig. 7 permits to analyse how good the load-displacement curve approximates the experimental diagram in terms of the reference points used in each case; in these diagrams, the initial part of the load-displacement diagram is shown and the reference points are depicted in red. Although Approach 1 clearly overestimates the peak load, it provides a very good approximation in terms of the reference points used in the calibration. Approaches 2 and 3 also provide a quite good general approximation in the reference points, but this figure allows to explain where the main differences of the result provided by each approach come from. For example, although Approach 1 reaches a very close approximation in the reference points, since only four points are used, the accuracy of the rest of the diagram is simply not taken into account, that is why some key points, such as the initial peak load, is not correctly obtained. In this case, the numerical diagram adjusts well the first reference point, which identifies the initial peak load, but reaches a higher peak afterwards. In the case of Approach 2, the initial peak load is not correctly captured simply because the first reference point is after it, so it is not taken into account; the rest of the diagram is properly reproduced. Finally, Approach 3 provides the best of the three results because it uses the reference points of both, thus takes into account the peak load and, due to the additional reference points, such as the second, limits the possibility of reaching higher peak loads afterwards, as observed in Approach 1.

If the accuracy of the calibration is analysed in terms of the deviation factor, Fig. 8 shows the evolution of the deviation factor λ along the calibration process, computed for each of the 200 models used in the

iterative process in each approach. The figure on the left shows the evolution of λ computed as expressed by Eq. (3) and the figure on the right shows a normalised value of obtained by dividing it by λ_0, which corresponds to the value of λ in the first iteration. In all three approaches, a good approximation is obtained after 100 iterations. In the case of Approach 1, the deviation factor is close to zero, especially if compared with Approaches 2 and 3; this does not imply that Approach 1 is better, as has been commented on before, but only that Approach 1 allows obtaining a lower value of λ simply because the numerical result has to be approximated in only four points, while in Approaches 2 and 3, approximation is carried out in 100 and 104 points, repectively.

The errors of the calibrated models considering the criterion based on the released energy, computed as the areas under the load-displacement diagrams according to Eq. (4), are 3.45%, 0.87% and 1.27% for Approaches 1, 2 and 3, respectively.

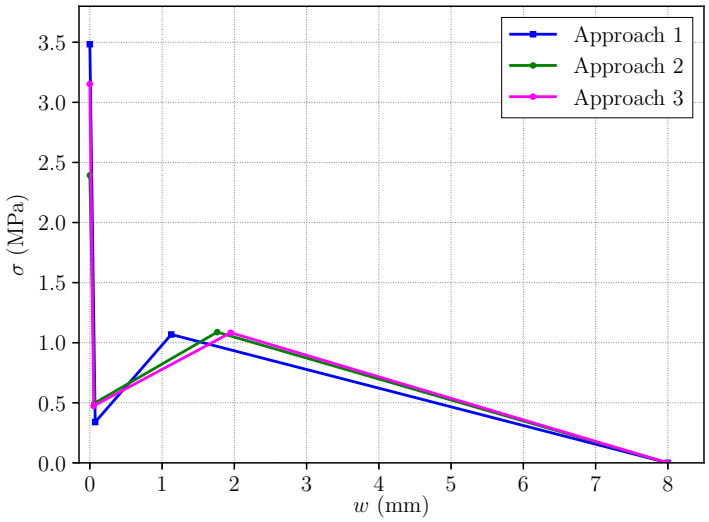

Figure 5: Resulting trilinear diagrams using different reference points (Approaches 1 to 3).

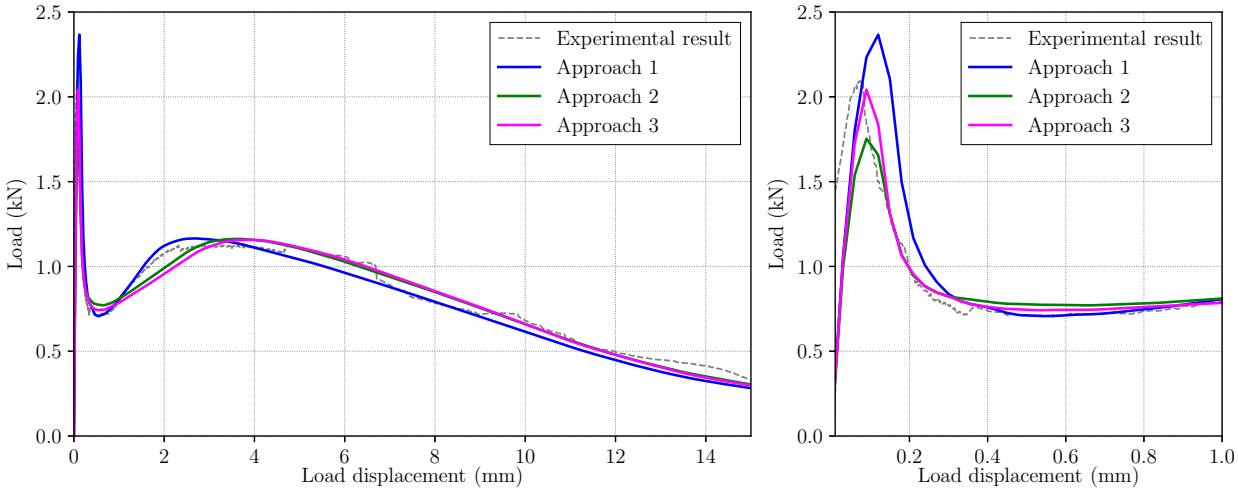

Figure 6: Result of the automated calibration process using different reference points (Approaches 1 to 3); full load-displacement diagram (left) and detail around the initial peak load (right).

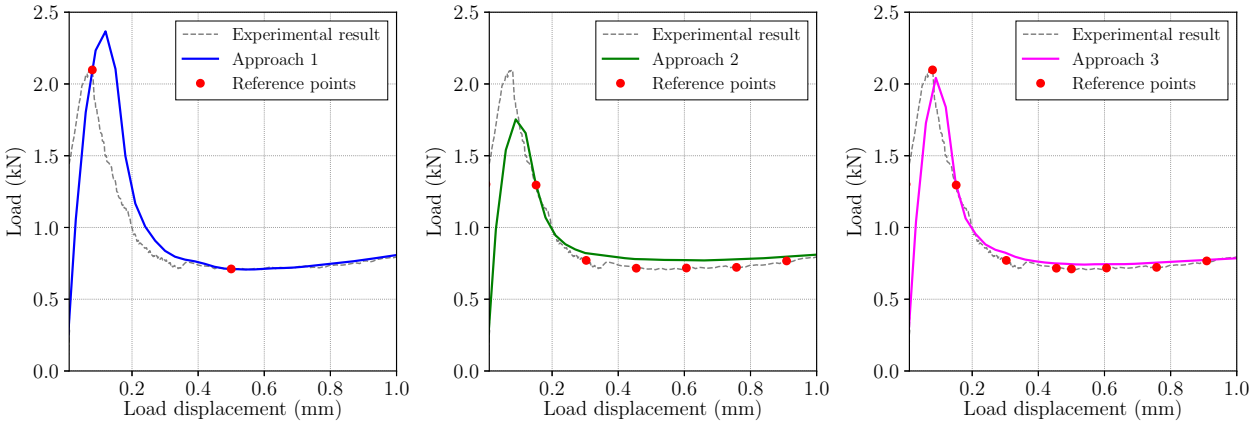

Figure 7: Comparison between the calibration result and the experimental diagram at the reference points (marked in red) in Approaches 1 to 3.

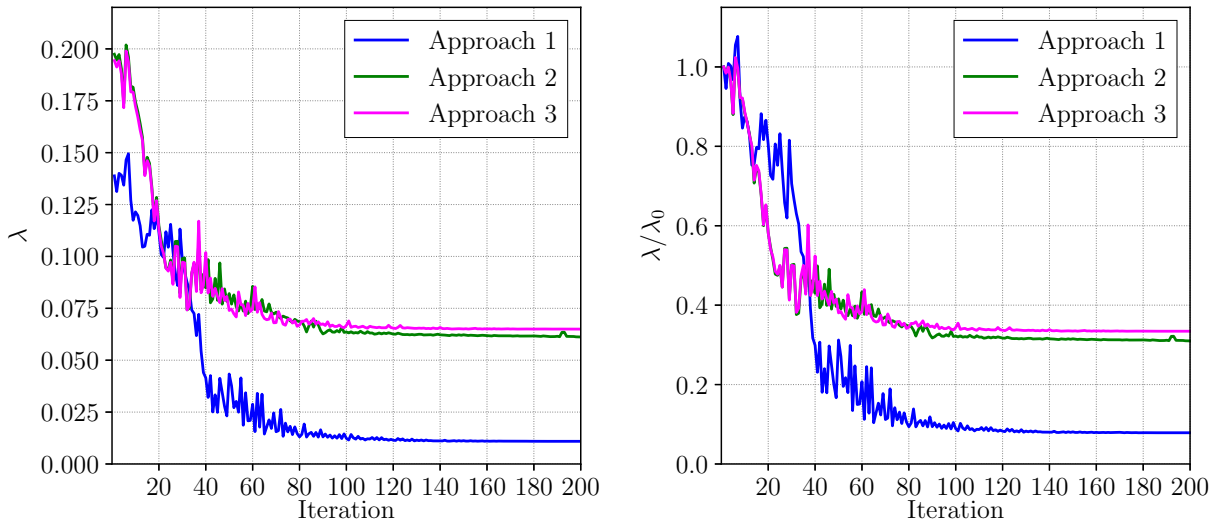

Figure 8: Evolution of the deviation factor λ using different reference points; left: original definition of the deviation factor (Eq. (3)), right: normalised value of the deviation factor (λ/λ_0, with λ_0 being the value of λ at the beginning of the iteration process).

4.1.2. Influence of weights on the calibration process

In this section the influence of weights used to evaluate the deviation factor is analysed. In principle, weighting the influence of the reference points may lead to a calibration result where some points are more relevant than others. Since the four reference points used in Approach 1 identify key points of the load-displacement diagrams, these four points are always weighted with a factor equal to 1 while other points are weighted with factors lower than 1. Therefore, using Approach 3 as a reference, since it was the best approximation obtained in the first set of approaches, analysed in the previous section, Approaches 4, 5 and 6 use a weighting factor of 1 for the four key reference points of Approach 1 and weighting factors of 0.5, 0.25 and 0.1, respectively, for the other 100 evenly distributed reference points.

Fig. 9 shows the resulting trilinear diagrams and Fig. 10 the load-displacement curves obtained in each case compared with the experimental diagram that is used for adjustment. In all cases, the calibration process produces an overall good adjustment, although relevant differences may be observed around the initial peak. If the detail of the diagrams shown at the right diagram of Fig. 10 is observed, Approaches 3 and 4 provide very similar results, in both cases the peak load is close to the experimental value. Nevertheless, Approaches 5 and 6 show less accurate peak values, thus showing that the peak value is less accurate as the weighting factor of the evenly distributed reference points becomes lower. This can be easily explained, since reducing the relevance of the evenly distributed points on the calibration process through the computation of the deviation factor λ is ultimately leading to a calibration scheme similar to Approach 1, where only four key points were considered.

Fig. 11 shows the evolution of the deviation factor in each case, both using the original expression of λ from Eq. (3) and its weighted expression (λ/λ_0). In all cases, the calibration process leads to a good result around iteration 100 and, if the weighted diagrams are considered, no important differences may be observed.

The errors of the calibrated models using Eq. (4) are 1.27%, 1.25%, 1.53% and 1.10% for Approaches 3, 4, 5 and 6, respectively.

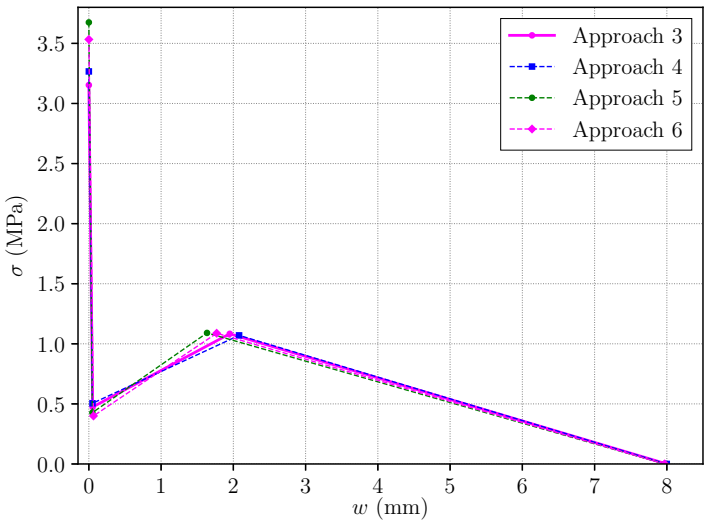

Figure 9: Resulting trilinear diagrams using different weights on the same reference points (Approaches 3 to 6).

4.1.3. Influence of careful selection of the reference points on the calibration process

To analyse the influence of a good selection of the reference points, rather than selecting a large number of them or using different weighting factors to modify their influence on the calibration process, Approach 7 uses the four key reference points of Approach 1 and ten additional reference points carefully selected at the following displacements: 0.05, 0.15, 0.2, 0.25, 0.7, 1.5, 2, 2.5, 6 and 10. This selection of reference points aims to obtain a better adjustment in the first part of the diagram, where the initial peak load and the load drop after it are located. Figure 12 shows the numerical adjustment obtained with Approach 7, depicting the reference points used in red.

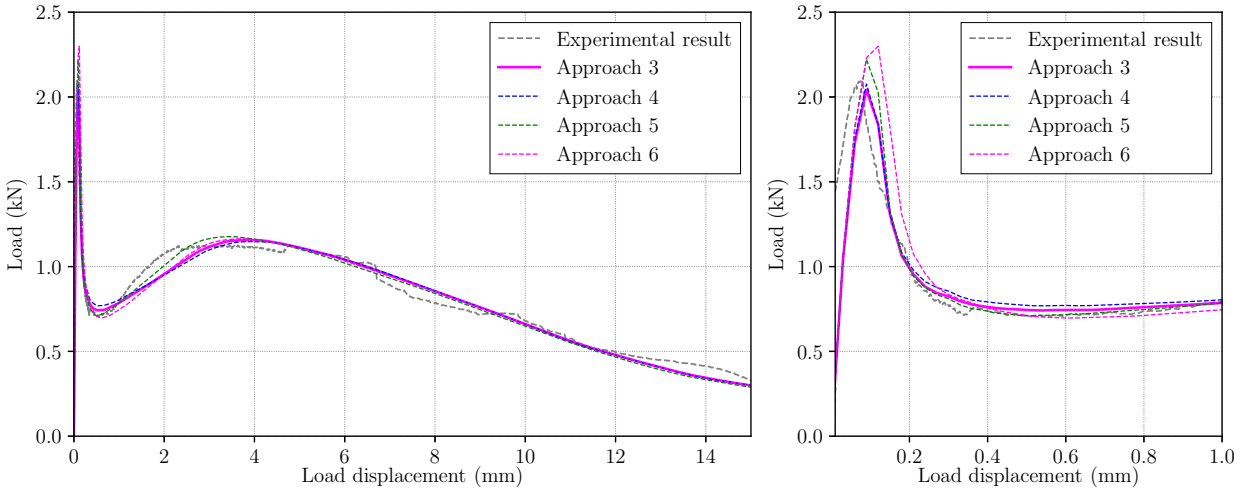

Figure 10: Result of the automated calibration process using different weights on the same reference points (Approaches 3 to 6); full load-displacement diagram (left) and detail around the initial peak load (right).

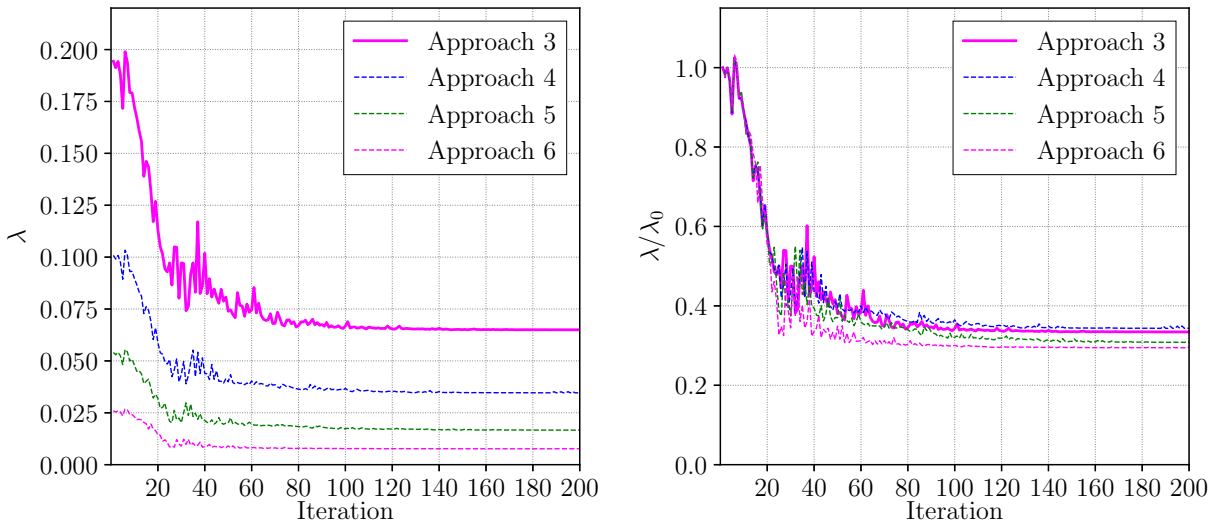

Figure 11: Evolution of the deviation factor λ using different weights on the same reference points (Approaches 3 to 6); left: original definition of the deviation factor (Eq. (3)), right: normalised value of the deviation factor (λ/λ_0, with λ_0 being the value of λ at the beginning of the iteration process).

The load-displacement diagram obtained with this approach shows a good adjustment, especially around the initial peak load and subsequent load drop, where other approaches provided not such an accurate adjustment. The rest of the diagram also shows a good adjustment.

In this case, the error of the calibrated model using Eq. (4) is 0.37%.

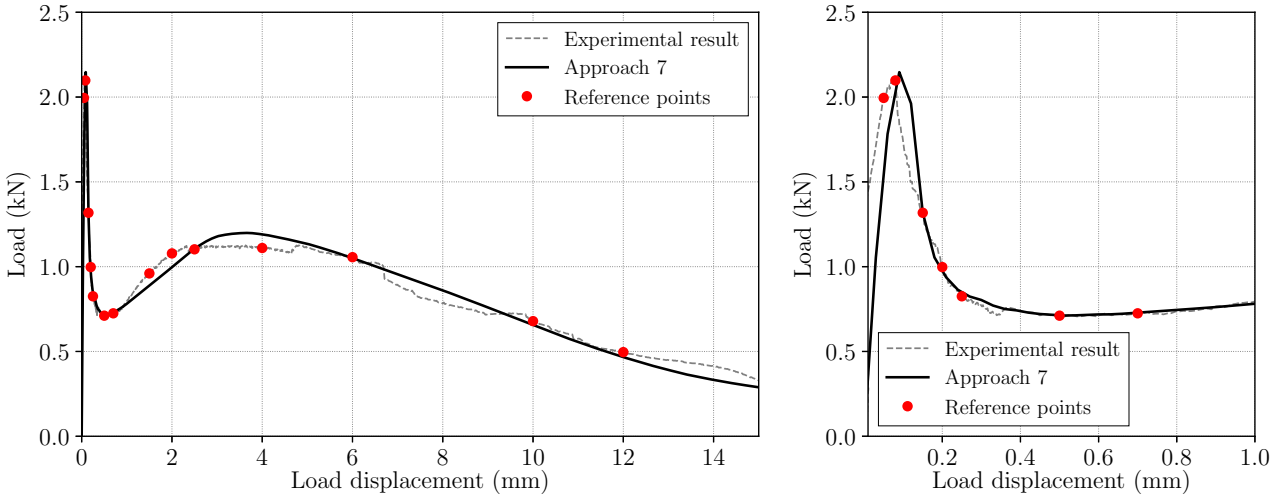

Figure 12: Result of the automated calibration process using carefully selected reference points (Approach 7); full load-displacement diagram (left) and detail around the initial peak load (right).

4.2. Influence of the mesh on the calibration result

A good design of the mesh is usually of utmost importance when numerically reproducing nonlinear problems with the finite element method. In order to analyse how some key aspects of the mesh design may modify the calibration result, this section analyses the mesh size in the region of fracture and the use of different types of elements.

Four models are analysed, all of them with the same specimen geometry as in Section 4.1 and using the same initial guess of the material parameters to be calibrated. Three models, identified as T4, T8 and T16, have triangular three-node elements in the region of fracture with element sizes of 4, 8 and 16 mm, respectively. The fourth model, identified as Q8, has quadrangular four-node elements with an element size of 8 mm in the region of fracture. Figure 13 shows the meshes used in each of these models.

The influence of the element size can be analysed in Fig. 14, that presents the load-displacement diagrams for the three meshes with triangular elements; T4, T8 and T16 results are presented in blue, green and magenta, respectively. In all cases, the results match well with the experimental curve and no big differences can be observed.

With regard to the influence of the element type on the calibration result, Fig. 15 shows the load-displacement diagrams of T8 and Q8 meshes (represented with solid lines and dashed lines, respectively), resulting in very similar diagrams, both close to the experimental curve.

The errors of the calibrated models obtained with Eq. (4) are 0.45%, 1.29%, 0.81% and 0.08% for meshes T4, T8, T16 and Q8, respectively.

4.3. Validation with other geometries and mixes

In the previous sections the calibration procedure has been used with the same experimental result in all cases, therefore an only fibre-reinforced concrete mix and an only specimen geometry have been used up to this point. In order to validate the proposed procedure with other experimental results, in this section the calibration process is used to automatically calibrate other tests with different fibre-reinforced materials and with other specimen dimensions. More especifically, two results of steel fibre-reinforced concrete specimens (SFRC) with different fibre proportions and four results of polyolefin fibre-reinforced concrete specimens (PFRC), also with different fibre proportions, are used. The results of SFRC are extracted from [31] and

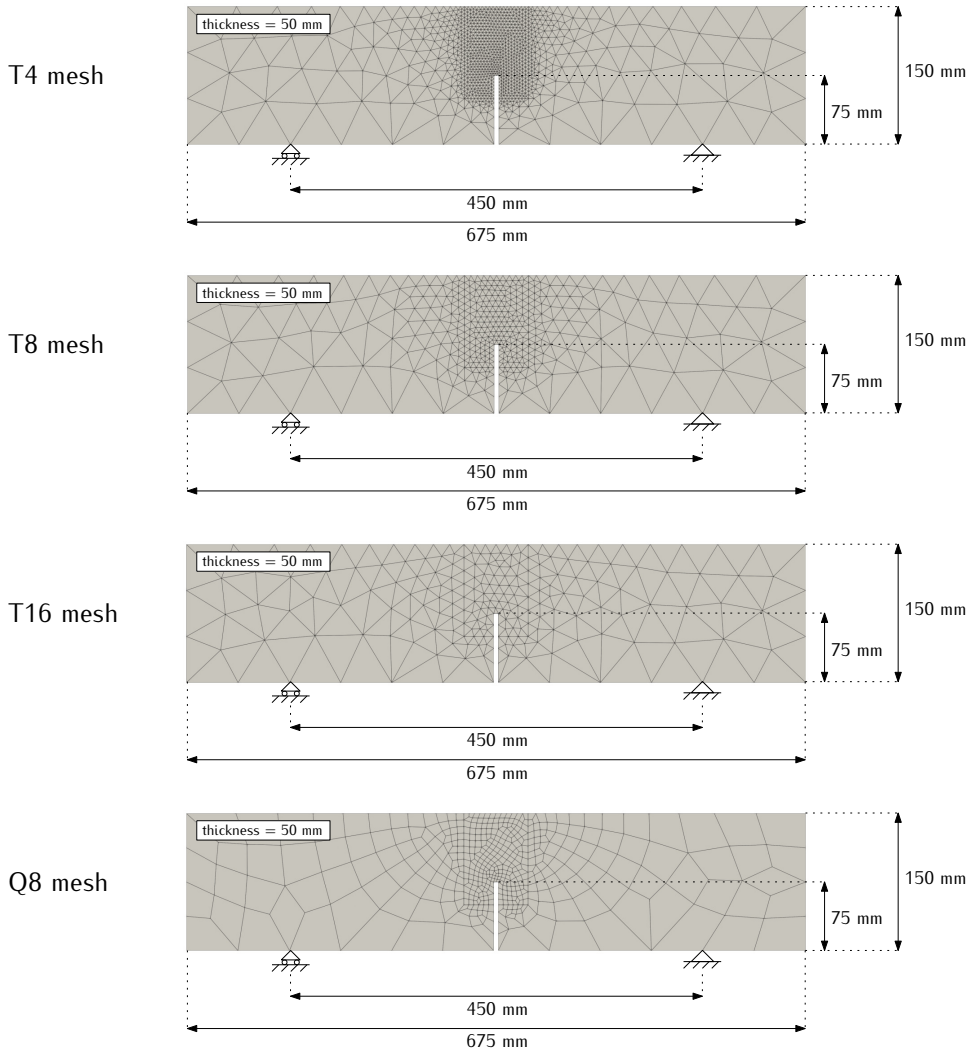

Figure 13: Meshes used to analyse the influence of the element size and the element type on the calibration result.

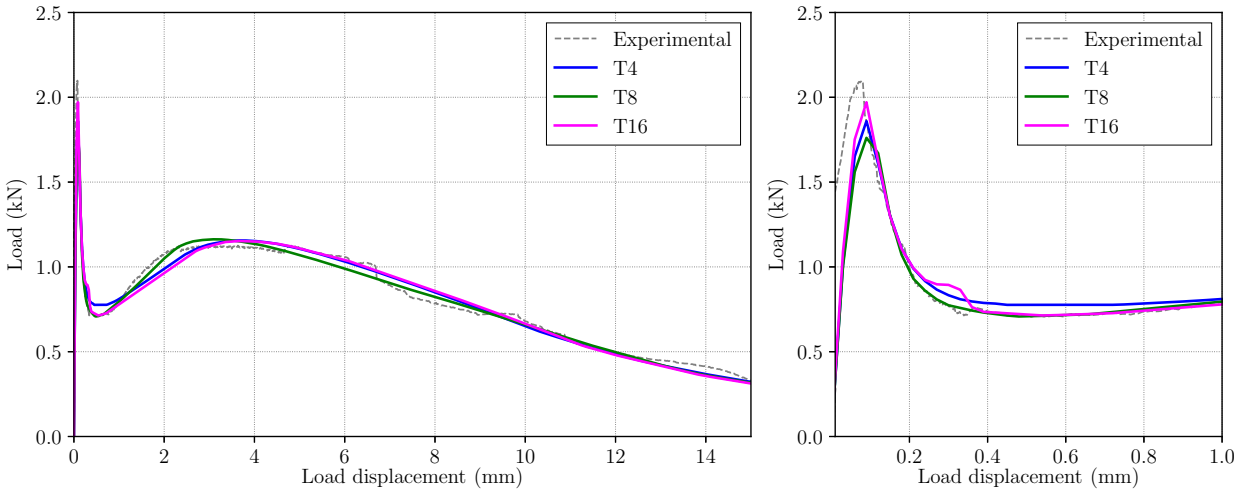

Figure 14: Result of the automated calibration process using three different element sizes in the region of fracture; full load-displacement diagram (left) and detail around the initial peak load (right).

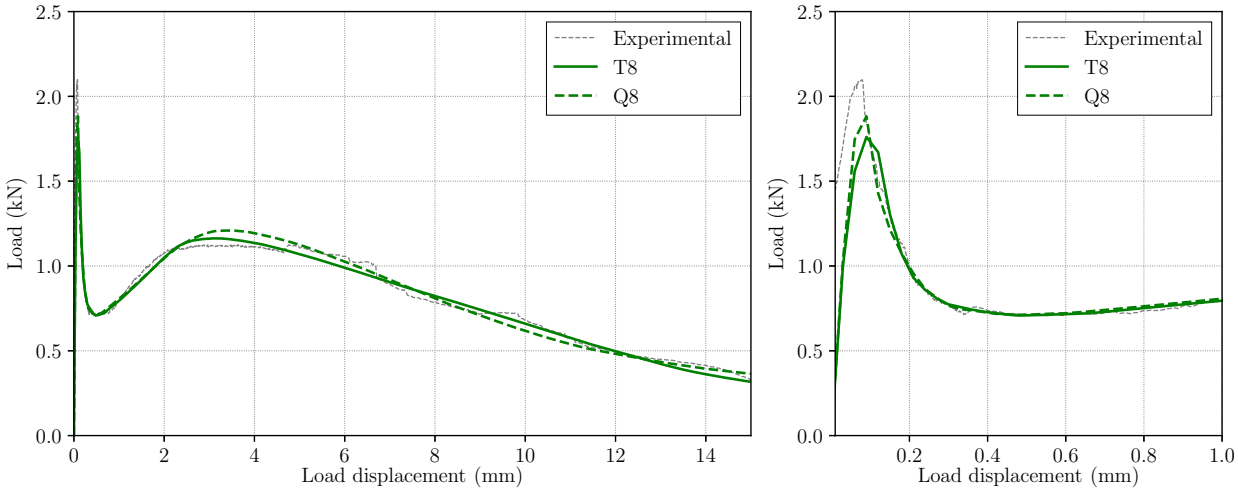

Figure 15: Result of the automated calibration process using different element types in the region of fracture; full load-displacement diagram (left) and detail around the initial peak load (right).

correspond to mixes with 30 and 45 kg of fibres per cubic metre of concrete; the specimens are 600 mm long and have a square cross section of 150 mm × 150 mm, with a notch of 75 mm and the test is carried out with a span of 450 mm. As for the results of PFRC, they are extracted from [11] and correspond to mixes with proportions of 3, 4.5, 6 and 10 kg of fibres per cubic metre of concrete; the specimens' dimensions are 430 in length, 100 mm in height and 100 mm in depth and have a notch of 33 mm and a testing span of 300 mm. Figure 16 shows the geometry of both specimens, as well as the triangular meshes used.

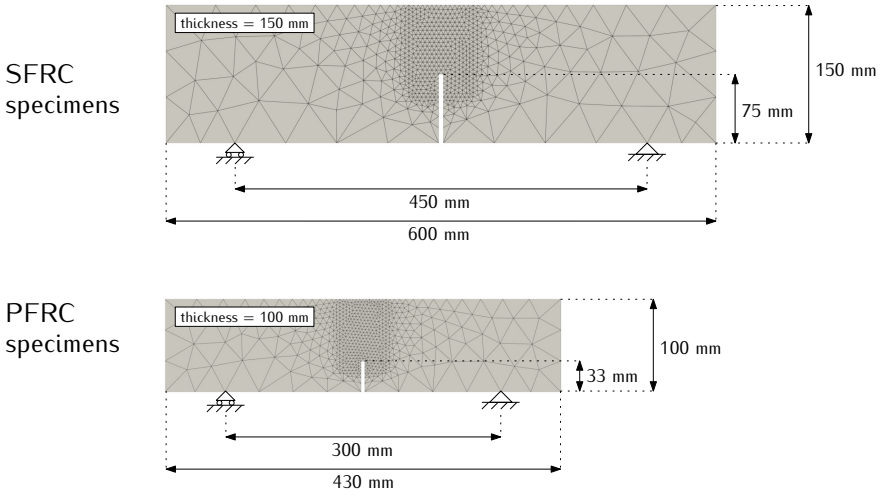

Figure 16: Meshes used to validate the calibration process with other specimen geometries and other materials (SFRC specimens from [31] and PFRC specimens from [11]).

The calibration results for these seven experimental results are presented in Fig. 17 and Fig. 18. In all cases, the numerical model is calibrated using the average experimental diagram, which is shown in the figures for each set of tests, and the initial guess of the set of parameters to be calibrated are the same as used before, that is to say: $\varepsilon_0 = 1.418 \cdot 10^{-4}$, $f_k = 0.57$ MPa, $f_r = 1.18$ MPa, $w_k = 0.09$ mm, $w_r = 1.65$ mm and $w_f = 6.0$ mm. In the case of the PFRC specimens, the bounds used for each parameter have been the same as before: $\varepsilon_0 \in [1 \cdot 10^{-4}, 1 \cdot 10^{-2}]$, $f_k \in [0.1, 1.5]$, $f_r \in [0.1, 2]$, $w_k \in [0.01, 0.5]$, $w_r \in [1, 3]$ and $w_f \in [4.5, 8]$, with stresses expressed in MPa and crack openings in mm. In the case of SFRC specimens, due to their remarkably different experimental behaviour, these bounds have been modified as follows: $\varepsilon_0 \in [1 \cdot 10^{-4}, 1 \cdot 10^{-2}]$, $f_k \in [0.1, 3]$, $f_r \in [0.1, 3]$, $w_k \in [0.01, 0.5]$, $w_r \in [0.6, 3]$ and $w_f \in [4.5, 15]$, also with stresses expressed in MPa and crack

openings in mm. In these calibration processes, between 65 and 100 control points have been used, carefully selected around key regions, such as the peaks and valleys of the load-displacement diagrams.

Figures 17 and 18 shows the calibration result for each of these six cases. All the numerical diagrams are well adjusted to the experimental curves, predicting correctly the overall behaviour and the maximum and minimum values of the curves.

All the errors computed with the criterion based on the released energy, computed as the areas under the load-displacement diagrams (Eq. (4)), are smaller than 2%; more precisely 0.00%, 1.16%, 0.74% and 1.84% in the case of PFRC 3, PFRC 4.5, PFRC 6 and PFRC 10 specimens, while the errors are of 1.30% and 1.34% in the case of SFRC 30 and SFRC 45 specimens.

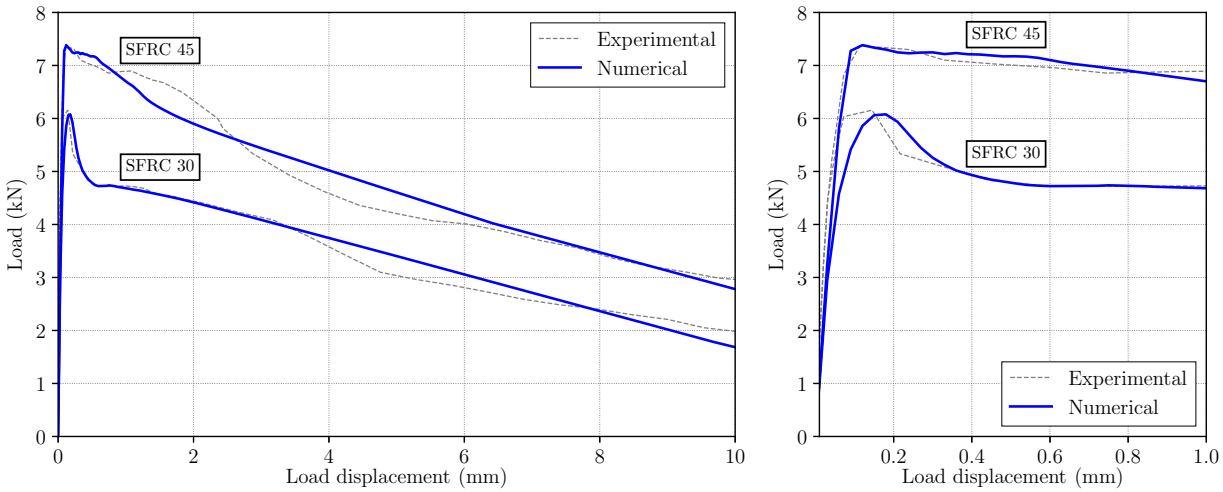

Figure 17: Result of the automated calibration process using different element types in the region of fracture; full load-displacement diagram (left) and detail around the initial peak load (right).

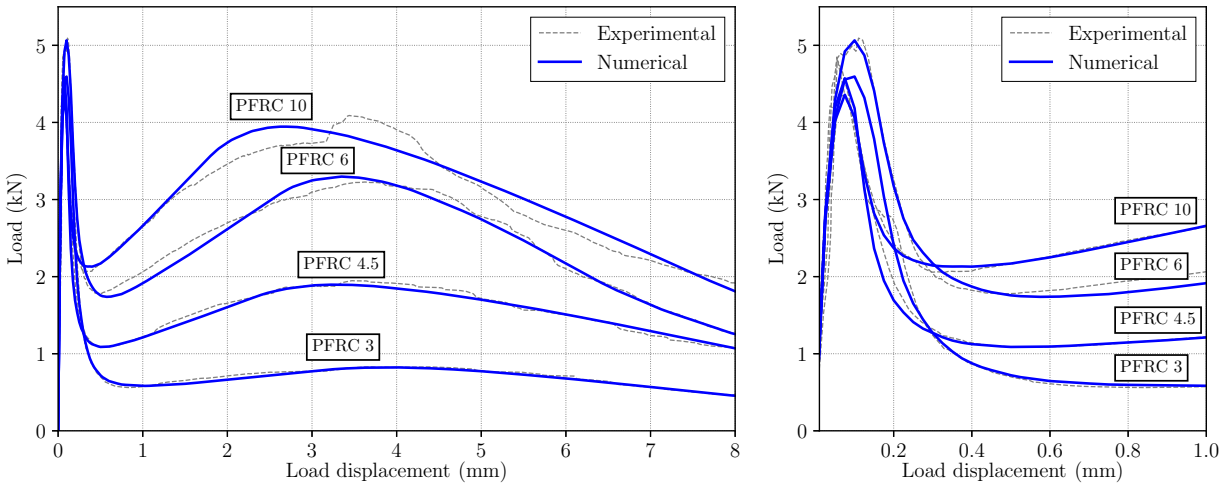

Figure 18: Result of the automated calibration process using different element types in the region of fracture; full load-displacement diagram (left) and detail around the initial peak load (right).

5. Summary and conclusions

This work has presented an automated calibration process for characterising the fracture behaviour of materials with complex behaviour, such as FRC. In this case, the model to calibrate consisted of a trilinear

diagram where six parameters need to be defined. Two results are compared, an experimentally obtained load-displacement diagram, that serves as reference, and a numerically produced load-displacement diagram obtained with a FEM model. The calibration is obtained through an iterative process where the material parameters are progressively modified in search of a numerical curve that is close enough to the experimental result. In this case, the process makes use of the Nelder-Mead algorithm, which minimises the so-called deviation factor, a value that assesses the quality of the approximation of the numerical result compared with the experimental curve. This process has proven to be effective and provides a good approximation, thus reducing the time needed to calibrate a model.

Several approaches have been analysed in order to understand how some key aspects of the process affect the result. To evaluate the adjustment quality of the numerical result, the deviation factor is computed using specific reference points in the load-displacement diagram. If only a few representative points are selected, the overall result is good, but some key aspects are not correctly described, as observed with the initial peak load of Approach 1. Nevertheless, the number of reference points is not the only important aspect in this matter, since correctly selecting them is equally important, as results of Approaches 2 and 3 proves. These two approaches use a similar number of reference points (100 and 104 in each case), but the accuracy of Approach 3 is clearly higher around the initial peak load, where Approach 2 clearly lacks accuracy, due to the fact that no reference points are selected around the initial peak in this case.

A second set of approaches (Approaches 3 to 6) have analysed the possibility of using different weights for the reference points, with the aim of making some points more relevant in the calibration process. Approaches 4 to 6 are similar to Approach 3, in all cases 104 reference points are used, but with a different weighting factor in 100 of them, which are evenly distributed along the experimental diagram used as reference. This comparison proves that all approaches provide a good adjustment, but differences mainly around the initial peak load are observed. As the evenly distributed points have lower weighting factors, their influence becomes lower and the calibration process tends to result in a similar adjustment as the one obtained with Approach 1, where only four key reference points were considered.

Finally, Approach 7 uses the proposed calibration process employing the same weighting factor with all reference points and making a careful selection of them, where the four key reference points used in Approach 1 are included and ten additional points are considered, most of them gathering around the initial part of the diagram, where the most significant load fluctuations are observed. This approach provides a good adjustment around the initial peak load and the load decay after peak, with a good general adjustment in the rest of the diagram.

Additionally, key aspects regarding the mesh design in the FEM model, such as the element size and the use of triangular or quadrangular elements in the region of fracture, have been analysed and the calibration procedure has been validated with other results found in the literature, including other type of fibres and different fibre proportions.

As a results of these studies, the following conclusions can be drawn:

- The proposed calibration procedure helps finding a set of material parameters that correctly adjusts the numerical model using a reference experimental diagram.
- The selection of the reference points strongly influences the result of the numerical adjustment. If key points are missing, the numerical result is not able to correctly reproduce some parts of the diagram.
- The use of different weighting factors in some reference points in order to make them more influential in the calibration process is effective, although it has not revealed as very relevant to obtain a good adjustment.
- A careful selection of the reference points helps to provide a better adjustment in key parts of the diagram and greatly helps to obtain a good adjustment in the key parts of the diagram.
- The calibration procedure is consistent even using coarse meshes.
- The calibration result provides a good approximation to the experimental diagram with triangular and quadrangular elements.
- The proposed procedure can be used to automatically calibrate different types of FRC specimens, providing good results with fibres and proportions with very different behaviour.

Data availability

All the `Python` code used for carrying out the calibration processes presented in this work, including the experimental diagrams used for comparison and the OOFEM finite element models, can be found on GitHub at the following link: `https://github.com/fernandosuarezguerra/acp_FRC`.

Acknowledgements

The authors gratefully acknowledge the financial support provided by the Ministry of Science, Innovation and Universities of Spain through the Research Fund Project PID2023-149321OA-C33.

References

[1] Zollo RF. Fiber-reinforced concrete: an overview after 30 years of development. Cement and Concrete Composites. 1997;19(2):107-22. Available from: `https://www.sciencedirect.com/science/article/pii/S0958946596000467`.

[2] Sweden Standard SS812310: 2014. Svenska Institutet för Standarder (SIS)—Bygg och anläggning: Stockholm, Sweden; 2014.

[3] Código estructural: Anejos 1-18. Ministerio de Transportes, Movilidad y Agenda Urbana, Madrid, España; 2021.

[4] fib Model Code 2010. Fédération Internationale du Béton fib/International Federation for Structural Concrete: Paris, France. Ernst & Sohn, Wiley; 2013.

[5] China CECS38:2004. Technical Specification for Fiber Reinforced Concrete Structures provides Guidelines for Various Applications. Dalian University of Technology: Dalian, China; 2004.

[6] Oliver J, Linero DL, Huespe AE, Manzoli O. Two-dimensional modeling of material failure in reinforced concrete by means of a continuum strong discontinuity approach. Computer Methods in Applied Mechanics and Engineering. 2008;197(5):332-48.

[7] Havlásek P, Kabele P. A detailed description of the computer implementation of SHCC material model in OOFEM. CTU in Prague. 2017.

[8] Lamus FA, Linero DL, Guevara RD. Two-Dimensional Numerical Model of the Fracture Process in Steel Fibre Reinforced Concrete with the Continuum Strong Discontinuity Approach and Functional Data Analysis. Latin American Journal of Solids and Structures. 2019;16:e180.

[9] Carvalho MR, Barros JAO, Zhang Y, da Costa DD. A computational model for simulation of steel fibre reinforced concrete with explicit fibres and cracks. Computer Methods in Applied Mechanics and Engineering. 2020;363:112879. Available from: `https://www.sciencedirect.com/science/article/pii/S004578252030061X`.

[10] Suárez F. A smeared crack formulation for simulating fracture of fibre-reinforced concrete by means of a trilinear softening diagram. Engineering Fracture Mechanics. 2023;288:109356. Available from: `https://www.sciencedirect.com/science/article/pii/S0013794423003144`.

[11] Alberti M, Enfedaque A, Gálvez J, Reyes E. Numerical modelling of the fracture of polyolefin fibre reinforced concrete by using a cohesive fracture approach. Composites Part B: Engineering. 2017;111:200-10.

[12] Suárez F, Gálvez J, Enfedaque A, Alberti M. Modelling fracture on polyolefin fibre reinforced concrete specimens subjected to mixed-mode loading. Engineering Fracture Mechanics. 2019;211:244-53.

[13] Suárez F, Gálvez JC, Alberti MG, Enfedaque A. Fracture and Size Effect of PFRC Specimens Simulated by Using a Trilinear Softening Diagram: A Predictive Approach. Materials. 2021;14(14). Available from: `https://www.mdpi.com/1996-1944/14/14/3795`.

[14] Nour A, Massicotte B, De Montaignac R, Charron JP. Development of an inverse analysis procedure for the characterisation of softening diagrams for FRC beams and panels. Construction and Building Materials. 2015;94:35-44.

[15] Barros JA, Cunha VM, Ribeiro AF, Antunes J. Post-cracking behaviour of steel fibre reinforced concrete. Materials and Structures. 2005;38:47-56.

[16] de Oliveira e Sousa JLA, Gettu R. Determining the tensile stress-crack opening curve of concrete by inverse analysis. Journal of engineering mechanics. 2006;132(2):141-8.

[17] Vincenzi L, Gambarelli P. A proper infill sampling strategy for improving the speed performance of a surrogate-assisted evolutionary algorithm. Computers & Structures. 2017;178:58-70.

[18] Vincenzi L, Ponsi F, Bassoli E, Buratti N. A computationally efficient procedure for calibrating model parameters of multiple specimens. Construction and Building Materials. 2024;411:134757.

[19] Stephen SJ, Raphael B, Gettu R, Jose S. Determination of the tensile constitutive relations of fiber reinforced concrete using inverse analysis. Construction and Building Materials. 2019;195:405-14.

[20] Kwon SH, Zhao Z, Shah SP. Effect of specimen size on fracture energy and softening curve of concrete: Part II. Inverse analysis and softening curve. Cement and Concrete Research. 2008;38(8-9):1061-9.

[21] Reddy KC, Subramaniam KV. Analysis for multi-linear stress-crack opening cohesive relationship: Application to macro-synthetic fiber reinforced concrete. Engineering Fracture Mechanics. 2017;169:128-45.

[22] Savoia M, Ferracuti B, Vincenzi L. Inverse analysis for the calibration of FRP—concrete interface law. Advances in Structural Engineering. 2009;12(5):613-25.

[23] Enfedaque A, Alberti MG, Gálvez JC, Domingo J. Numerical simulation of the fracture behaviour of glass fibre reinforced cement. Construction and Building Materials. 2017;136:108 117. Available from: `http://www.sciencedirect.com/science/article/pii/S0950061816320517`.

[24] Patzák B. OOFEM—an object-oriented simulation tool for advanced modeling of materials and structures. Acta Polytechnica. 2012;52(6).

[25] Virtanen P, Gommers R, Oliphant TE, Haberland M, Reddy T, Cournapeau D, et al. SciPy 1.0: Fundamental Algorithms for Scientific Computing in Python. Nature Methods. 2020;17:261-72.

[26] Oliver J. A consistent characteristic length for smeared cracking models. International Journal for Numerical Methods in Engineering. 1989;28(2):461-74.

[27] Nelder JA, Mead R. A simplex method for function minimization. The computer journal. 1965;7(4):308-13.

[28] Conn AR, Gould NI, Toint PL. Trust region methods. SIAM; 2000.

[29] Wright SJ. Numerical optimization; 2006.

[30] Alberti M, Enfedaque A, Gálvez J. Comparison between polyolefin fibre reinforced vibrated conventional concrete and self-compacting concrete. Construction and Building Materials. 2015;85:182-94.

[31] Barros JA, Figueiras JA. Flexural behavior of SFRC: testing and modeling. Journal of materials in civil engineering. 1999;11(4):331-9.